Experimental Detection of Early-Stage of Lung and Skin Tumors based on Super Wideband Imaging

Wasan Alamro, *Student Member, IEEE*, Boon-Chong Seet, *Senior Member, IEEE*, Lulu Wang, *Member, IEEE*, and Prabakar Parthiban, *Member, IEEE*

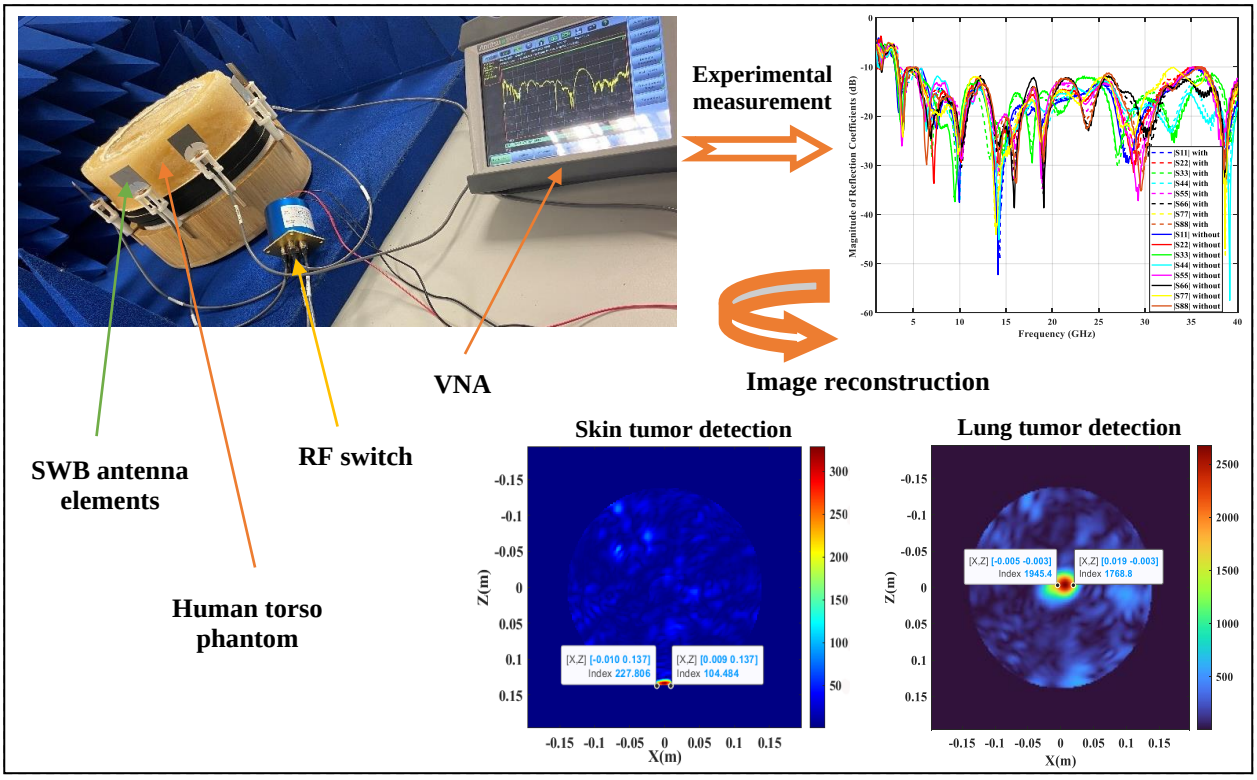

Super wideband (SWB) imaging approach for lung and skin tumor detection evaluated by experimental measurement and image reconstruction on human torso phantom.

Take-Home Messages

- This paper proposes for the first time a super wideband (SWB) imaging approach for accurate detection of deep-seated lung and in-situ skin tumors.
- The proposed approach demonstrates a significant enhancement in spatial resolution of tumor imaging over present ultra-wideband (UWB) approach.
- Our approach targets cancer detection through accurate imaging of early-stage malignant tumors from deep-seated to superficial locations.
- To the best of our knowledge, we are the first to propose, develop, and experimentally evaluate the SWB imaging approach for early-stage tumor detection.
- By virtue of the super-wide bandwidth, our approach could help realize a multi-cancer type detection system for different tumor types and locations in a contactless manner.

Experimental Detection of Early-Stage Lung and Skin Tumors based on Super Wideband Imaging

Wasan Alamro, *Student Member, IEEE*, Boon-Chong Seet, *Senior Member, IEEE*, Lulu Wang, *Member, IEEE*, and Prabakar Parthiban, *Member, IEEE*

Abstract In this paper, a super wideband (SWB) radio frequency imaging approach is developed and evaluated for detecting early stages of deep-seated lung and in-situ skin tumors. A life-sized human torso phantom is constructed of tissue mimicking materials and their dielectric properties are thoroughly investigated over the covered frequency range of 3.1–40 GHz. An array of custom-designed antenna elements is employed in an imaging setup to assess the detection capabilities of the SWB imaging approach for both lung and skin tumors. Images reconstructed using the acquired backscattering information and confocal beamforming algorithms demonstrate a successful detection with accurate tumor size and location estimation. Compared to present ultra-wideband (UWB) approach, the proposed SWB approach can enhance the spatial resolution of the reconstructed images by up to 84.4%. This work establishes the foundation for further exploration of SWB imaging in clinical trials, offering the potential to transform early cancer detection and treatment monitoring.

Keywords **— Early-stage tumor detection, deep-seated lung tumor, in-situ skin tumor, super-wideband imaging.**

I. Introduction

RADIO frequency (RF) based imaging at microwave and millimeter wave frequencies has seen increased attention in the past few years. It is considered a promising alternative to conventional means of detecting cancerous and severe diseases owing to its being contactless, use of non-ionizing radiation, relatively low cost, and non-invasive [1], [2]. The dielectric contrast between healthy and unhealthy tissues is the basis of RF imaging for detecting cancer [3] such as breast cancer [4], [5], [6], brain stroke and tumors [7], [8], [9], [10], and critical health conditions such as chest fluid accumulation [11], [12], [13].

Lung and skin cancer may represent two extreme cases of cancer detection in terms of their tumor location: from the most deep-seated to the most superficial location. Lung cancer is one of the leading causes of cancer death in the world. Different stages of this disease are determined according to the tumor size and spread of the abnormal cell growth in human organs. On the other hand, melanoma is an acute skin cancer in which there is uncontrolled growth of pigment cells [14]. The progression of the disease unfolds in stages, commencing at stage 0 (in-situ) where the tumor is confined to the outermost skin layer, and advancing to stage 4 where the tumor spread beyond lymph nodes to other organs [15]. Early detection of lung and skin cancer is crucial for successful treatment and preventing further spread of cancerous tissues. While common detection methods such as computed tomography (CT) scans and X-rays are utilized for detection and treatment monitoring, their cumulative radiation exposure presents inherent health risks. Consequently, there is an urgent need for a detection tool that is both safer and more cost-effective for detecting lung and skin cancers [16], [17], [18], [19].

Several studies have explored RF based imaging for cancer detection in deep-seated locations [20], [21], [22], [23], [24], [25]. However, there were limitations. For instance, one study [20] used low-gain antennas, limiting detection to superficial locations without size determination. Another study [21] used non-life-size lung phantom that did not consider the nature of tissue arrangement, resulting in weak signal penetration and low-resolution images. In [22], a life-size chest phantom was employed, but the tissue-equivalent liquids used do not mimic real tissue properties. Additionally, the work in [23] investigated lung tumors using unrealistic phantoms, while those in [24] and [25] used lung phantoms that lacked the rib bone layers.

Research on RF based imaging for skin cancer [26], [27], [28], [29], [30], [31] has also been conducted. In [26], a system comprising of four sub-UWB antipodal Vivaldi antennas to collectively achieve UWB imaging bandwidth is proposed. Although the system can detect tumors with high resolution, its achievable accuracy could be limited by the number of deployable antennas within a finite space, since it takes four sub-UWB antennas to provide the bandwidth of one UWB antenna. In [27], a UWB antenna is proposed to detect skin cancer on a four-layer forearm phantom. The imaging results demonstrate the effective identification of a 20 mm diameter tumor on the outermost skin layer. However, the detected tumor has a thickness comparable to that of the human skin layer, which implied that the tumor is not in its early stage and has spread through the whole skin layer. The authors in [28]

W. Alamro and B.-C. Seet are with Department of Electrical and Electronic Engineering, Auckland University of Technology, Auckland 1010, New Zealand; (e-mail: wasan.alamro@autuni.ac.nz, boon-chong.seet@aut.ac.nz).

L. Wang is with Biomedical Device Innovation Center, Shenzhen Technology University, Shenzhen 518118, China; (e-mail: wanglulu@sztu.edu.cn).

P. Parthiban is with Hardware Engineering Department, Services and Connectivity, Honeywell Aerospace, Yeovil BA20 2YD, UK; (e-mail: prabakarparthiban@gmail.com).

presented a wearable UWB antenna for skin cancer detection and used an artificial magnetic conductor to minimize radiation from the antenna deeper into the human body. It is simulation-only work with limited discussion on the imaging outcomes. In [29], a UWB approach was proposed to detect tumors on a phantom, which used a plastic cylinder to represent the skin layer without measurement of its dielectric properties in their frequency range of interest. The authors in [30] successfully detected tumor within the skin layer of the breast using an elliptical UWB antenna. However, the used phantom is a simplified one without representation of the tumor thickness and placement in the outer skin layer. To overcome the previously mentioned challenges, we have proposed SWB imaging for detecting different tumor types in different tissue layers of a multilayer realistic torso phantom.

Under these contexts, for the first time, we experimentally investigate the capabilities of the SWB imaging for medical applications. The imaging setup utilizes our custom-designed monopole SWB antenna [32], [33] that operates over a super-wide frequency range from 3.1 to 40 GHz (ratio bandwidth > 10:1). In [32], we studied the key performance parameters of our proposed SWB antenna in terms of reflection coefficient (S_{11}), gain, and radiation pattern. In [33], we conducted a thorough simulation study on utilizing an array of our SWB antennas for detecting lung tumor of different sizes and at different locations of the lung tissue. Building on the outcomes from these previous works, this paper further investigates experimentally the potential of an imaging system utilizing our SWB antennas for detecting not only lung, but also skin tumor, in a custom-built torso phantom composed of several tissue mimicking materials (TMMs). The specific objectives are to study the dielectric properties of the TMMs across the SWB frequency range, detect early stages of both deep-seated lung and in-situ skin tumors using life-size torso phantoms, and enhance spatial resolution and signal-to-clutter ratio (SCR) [34], [35], which are limited in conventional RF imaging systems due to bandwidth constraints [36].

The main contributions of this paper are:

- Development and experimental validation of a SWB imaging approach to significantly enhance the detection of early-stage deep-seated lung tumors. Unlike the previous studies, our work showcases the capability of SWB imaging to accurately locate and size early-stage tumors even in deep regions of a five-layer life-size torso phantom with thoroughly characterized dielectric properties across the entire bandwidth.
- Investigating the capability of SWB imaging to locate and size early-stage in-situ skin tumor in the epidermis (outermost skin layer) with smaller diameter and thickness, in contrast to existing studies that focus on skin tumors located at various depths of the skin or even extending into the adipose layer.
- Our work represents the first experimental study on SWB imaging for the detection of lung and skin tumors that represent two extreme cases of cancer detection in terms of their tumor location: from the most deep-seated to the most superficial location.
- Our work also represents the first experimental study on quantifying the change in detection accuracy due to the switch from UWB to SWB frequency range in the same imaging application.

The remainder of this paper is organized as follows: Section II details the methods used to measure the dielectric properties of the torso phantom across the SWB frequency range. Section III discusses the results obtained from imaging the torso phantom for the detection of lung and skin tumors. A performance comparison between the SWB and UWB imaging approaches is presented in Section IV. Finally, the concluding remarks are made in Section V.

II. Dielectric Properties of Torso Phantom

In order to build a phantom that mimics the composition and dielectric properties of human torso layers, experiments are conducted using different mixtures of TMMs [31] across the operating frequency range of our developed SWB antenna.

Utilizing the free space method [52], two identical antennas, T_x and R_x, covering the specified frequency range are employed. The antennas are separated by a distance of 760 mm, which is larger than the calculated minimum far-field distance. The measurement entails the utilization of a rectangular block of Material Under Test (MUT) with dimensions of 120 mm in length, 80 mm in width, and 40 mm in thickness, erected on a wooden platform with two antennas oriented towards it, each connected to a port of the vector network analyzer (VNA). The measurement involves firstly capturing the S-parameters of an empty platform positioned equidistantly between the antennas. The MUT is then placed on the platform with its width in the upright position, and the S-parameter measurement is repeated. The effect of the platform can be eliminated by employing a subtraction technique, allowing MUT's S-parameters such as transmission and reflection coefficients to be determined.

To process the measured S-parameters and extract MUT's dielectric properties, the Nicolson-Ross-Weir (NRW) method [37] is implemented. We opted for this method due to its being most common approach for extracting dielectric values from complex S-parameters recorded via the transmission/reflection method using a VNA. We obtained the Γ (reflection coefficient at interface) and P (propagation coefficient, a.k.a transmittance through dielectric layer) from S_{11} and S_{21} parameters, which then enable the extraction of MUT's complex relative permittivity, loss tangent, and conductivity [38]. We measured the dielectric properties of TMMs that constitute the human torso as listed in Table I. The measurement setup is shown in Fig. 1.

Fig. 2 represents the dielectric properties results of different TMMs over the frequency range from 1 to 40 GHz, where the relative permittivity tends to decrease with increasing frequency. However, the conductivity shows opposite behavior where it increases with frequency. It should be noted that the measured dielectric properties of the TMMs are within the range of the simulated results derived by Cole-Cole model [39], [40] of the corresponding torso tissues.

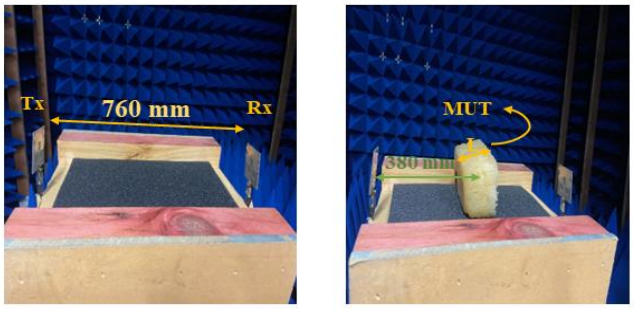

(a) (b)

Fig. 1. Setup for free space dielectric property measurement: (a) without MUT; and (b) with MUT.

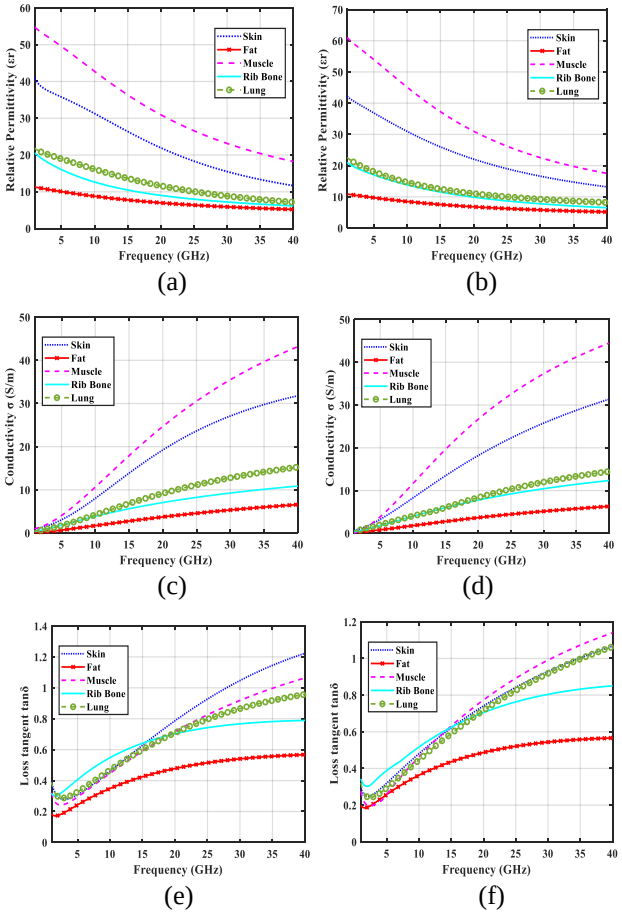

Fig. 2. Simulated Cole-Cole dielectric properties (left column); Measured dielectric properties (right column).

TABLE I
MEASURED DIELECTRIC PROPERTIES OF THE TORSO PHANTOM

Layers	Thickness (L)	TMMs (Ratio)
Skin	40 mm	Gelatine + Water (1:1.5) [21]
Fat	40 mm	Paraffin wax [41], [42]
Rib Bone (Cancellous)	15 mm	Plaster of Paris [43], [44]
Muscle	55 mm	Gelatine + Water (1:2.5) [21]
Lung (Inflated)	44 mm	Gelatine + Water (1:1) [21]

III. EXPERIMENTAL MEASUREMENTS

A. *Deep-Seated Lung Tumor Imaging*

For the purpose of detecting lung tumor located deep in the lung tissue, two human torso phantoms are constructed. One represents an unhealthy scenario where a tumour is present in the phantom, while the other represents a healthy scenario with no tumour present. The tumor is emulated with a 25 mm diameter red grape, which is considered in literature as a suitable equivalent to tumor tissue [45], [46]. In the lower frequency range of 2.45 GHz, the dielectric properties of fresh grapes are higher than those of healthy tissues, exhibiting a permittivity of ~ 70, loss factor of 17, and conductivity of 4 S/m. In comparison, the permittivity of tumors typically falls between 50–80, depending on tumor type and racial factors [47]. In the lung tissue, cancerous tumor can exhibit a relative permittivity and conductivity that are 2–3 times, and 1.6–2 times greater, respectively, than those of normal tissue [48], [49]. A significant contrast is observed between healthy and unhealthy skins, with the latter exhibiting permittivity levels 2–10 times higher than the former [30]. Hence, fresh grapes are considered a good representative for lung and skin tumors.

In Fig. 3, the dimensions of the constructed phantom and inserted tumor are shown. To set up for imaging, the phantom is positioned on a rotatable platform with a radius of 131 mm. A circular array of 8 elements of our custom-designed SWB antenna is positioned around the constructed phantom, each separated by an angle of 45°. A 10 mm separation is maintained between each element and phantom. The setup in Fig. 4 involves connecting port 1 of the VNA to an antenna element that functions as the transmit antenna, while port 2 is permanently connected to the common port of an electromechanical RF switch. By manual actuation of the electrical contact between the switch's common port and the port of each antenna element that functions as the receive antenna, backscattered signals received from the other 7 antenna elements connected to the RF switch are then recorded. Next, another antenna element is manually configured as the transmit antenna, and the measurement repeats until all elements have taken turns to function as the transmit antenna. Each measurement is repeated three times, and averaged value is used in the subsequent processing.

This process is executed for both healthy and unhealthy phantoms. The overall scan time of each phantom takes around 10–15 minutes. Following this, the recorded signals obtained using the healthy phantom are subtracted from those using the unhealthy phantom. The backscattered signals acquired from all antenna elements are compared over the operating frequency range of 3.1 to 40 GHz of our SWB antenna. The outcomes of this comparison are depicted in Fig 5.

The results indicate that the signals obtained from the unhealthy phantom exhibit higher reflection than those from the healthy phantom. This observation aligns with the expected behavior due to the higher dielectric properties of cancerous tissues caused by their higher water content. Notably, this distinction is most prominent at the initial resonant frequencies. In addition, a slight shift in frequency is observed, particularly

at the first resonance. As we sweep to higher frequencies, there is a decrease in signal penetration and increase in attenuation, which affect the signal behavior of both phantoms.

The recorded signals obtained from the antenna array are further processed using two beamforming algorithms: Delay and Sum (DAS); and Delay Multiply and Sum (DMAS). DAS is based on the coherent addition of the backscattered signals collected at different antenna positions, while DMAS is based on the antenna pair multiplication before the summation of reflected signals measured at different antenna positions [50]. Fig. 6 and Fig. 7 show the resulting reconstructed 2D images of the healthy, and unhealthy phantom, respectively, using DAS and DMAS, demonstrating the successful detection of the deep-seated tumor using both algorithms.

The size of the detected tumor is determined from the reconstructed images by identifying regions that represent high signal scattering, indicated in red on both color maps generated using DAS and DMAS algorithms. Generally, DMAS is found to yield a higher image resolution and more precise estimation of the tumor size compared to DAS, as detailed in Table II.

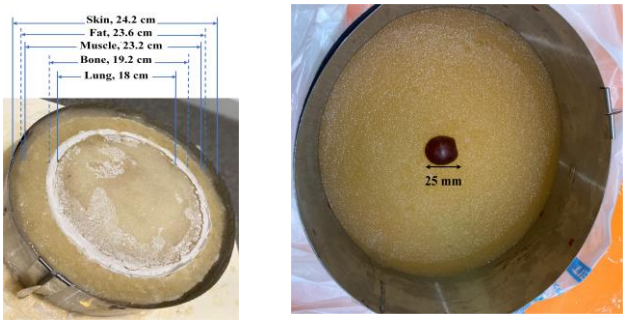

(a) (b)

Fig. 3. Constructed phantom of human torso: (a) phantom dimensions; and (b) inserted tumor.

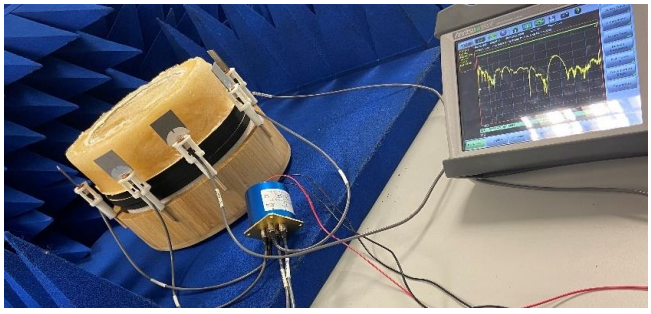

Fig. 4. Imaging setup for lung tumor detection.

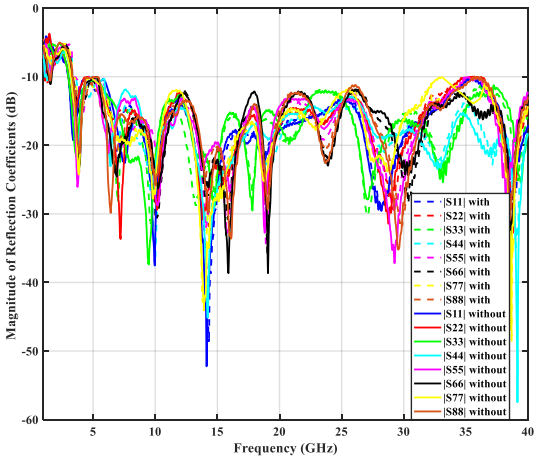

(a)

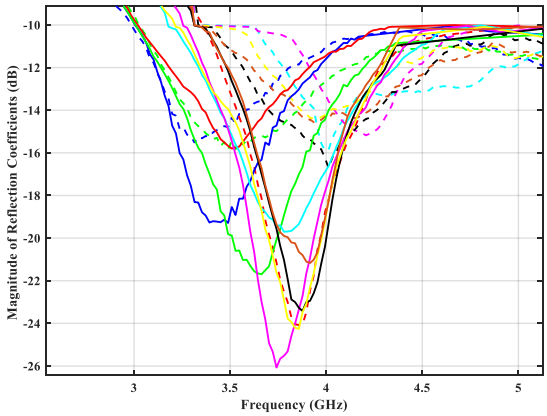

(b)

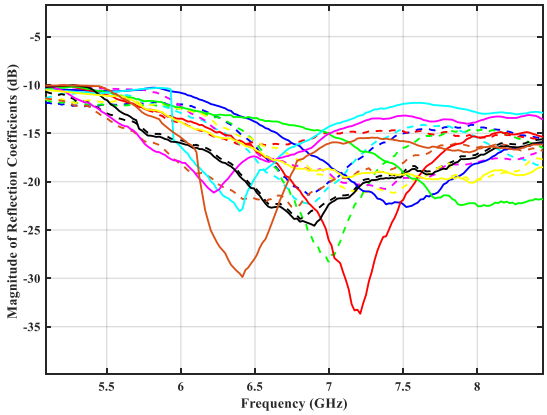

(c)

Fig. 5. (a) Comparison of measured reflection coefficients between healthy phantom (without lung tumor) and unhealthy phantom (with lung tumor) from all 8 antenna elements; (b) zoom-in view at first resonant frequency; (c) zoom-in view at second resonant frequency.

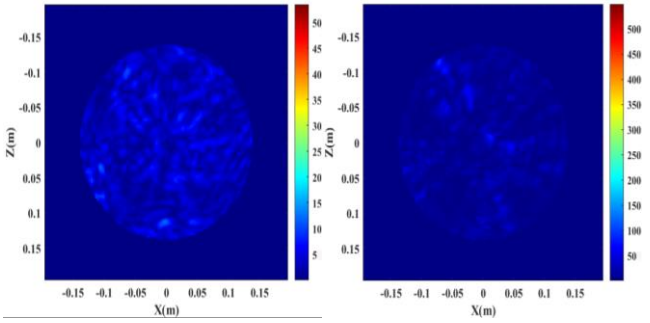

(a) (b)

Fig. 6. Reconstructed 2D images of healthy phantom using: (a) DAS; and (b) DMAS beamforming algorithms.

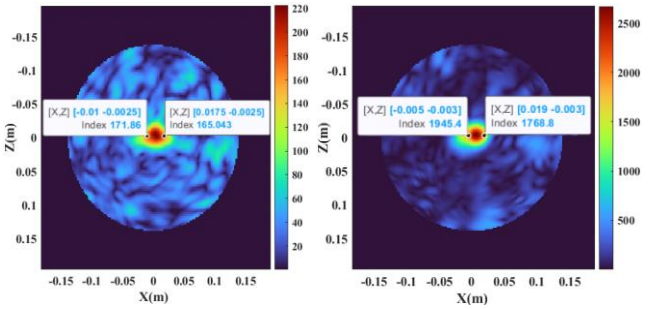

(a) (b)

Fig. 7. Reconstructed 2D images of unhealthy phantom with lung tumor using: (a) DAS; and (b) DMAS beamforming algorithms.

TABLE II

PERCENTAGE ERROR OF LUNG TUMOR DETECTION USING DAS AND DMAS

Beamforming algorithm	Real tumor diameter	Detected tumor diameter	Percentage Error
DAS	25 mm	27.5 mm	10%
DMAS	25 mm	24 mm	4%

B. In-Situ Skin Tumor Imaging

The same phantom composition for lung tumor detection is utilized to assess the SWB imaging approach in detecting in-situ skin tumor. As shown in Fig. 8, the measurement similarly involves the use of a healthy phantom and an unhealthy one with tumor inserted in the outermost skin layer of the torso phantom. The tumor is a grape slice of 20 mm diameter and 1 mm thickness. The corresponding imaging setup is illustrated in Fig. 9. The acquired reflection coefficient from the antenna directly facing the tumor (labeled Antenna 1) in the unhealthy phantom is compared with that from the healthy phantom as shown in Fig. 10. The results similarly show that the signals from the unhealthy phantom exhibit higher reflection than that from healthy phantom, and have their frequencies slightly shifted to a lower band, in particular at the first two resonances.

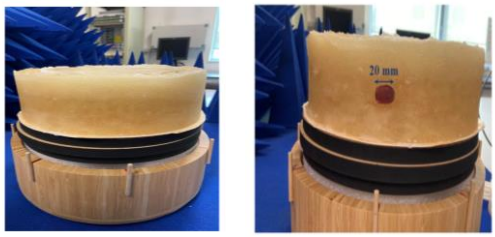

(a) (b)

Fig. 8. Constructed torso phantom: (a) healthy phantom; and (b) unhealthy phantom with skin tumor inclusion.

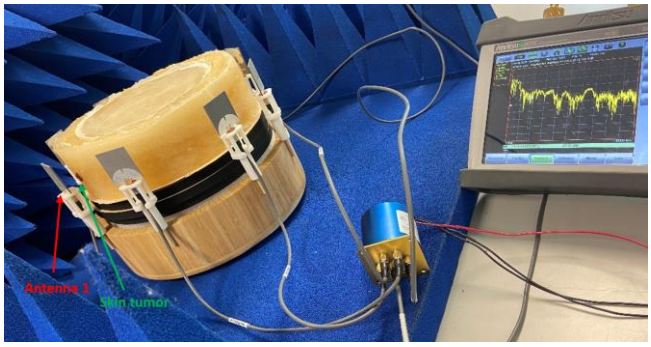

Fig. 9. Imaging setup for skin tumor detection.

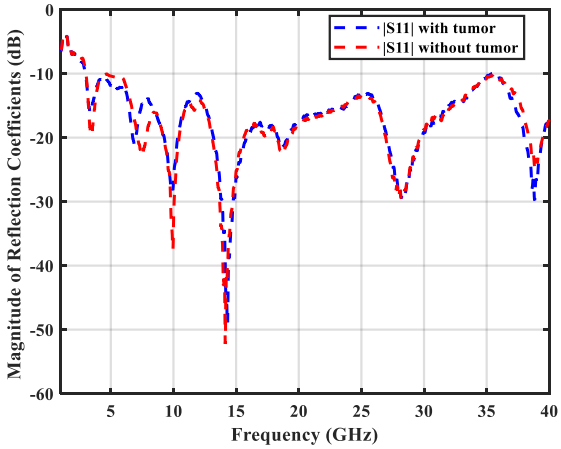

Fig. 10. Comparison of measured reflection coefficient between healthy phantom (without skin tumor) and unhealthy phantom (with skin tumor) at Antenna 1.

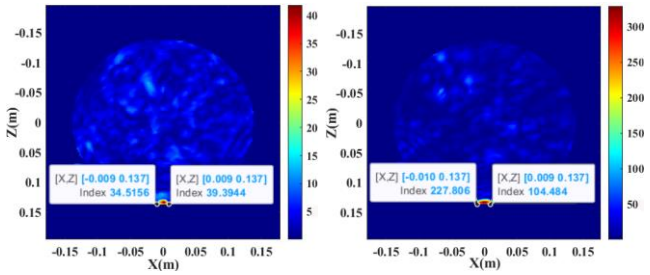

(a) (b)

Fig. 11. Reconstructed 2D images of unhealthy phantom with skin tumor using: (a) DAS; and (b) DMAS beamforming algorithms.

TABLE III
PERCENTAGE ERROR OF SKIN TUMOR DETECTION USING DAS AND DMAS

Beamforming algorithm	Real tumor diameter	Detected tumor diameter	Percentage error
DAS	20 mm	18 mm	10%
DMAS	20 mm	19 mm	5%

The corresponding reconstructed images in Fig. 11 clearly demonstrate the successful detection of skin tumor using both beamforming algorithms. Table III further shows that DMAS estimates the tumor size more accurately than DAS, proving again its capability in producing higher image resolution.

IV. SWB VS UWB IMAGING

In this section, we evaluate the impact of an antenna's bandwidth on the imaging performance by comparing the outcomes of utilizing super-wide imaging bandwidth to that of utilizing ultra-wide imaging bandwidth for lung tumor detection. We chose to compare in the context of detecting lung tumors as this type of cancer presents more detection challenges due to their deep-seated location. To enable a direct comparison between the two cases, instead of using a separate representative UWB antenna to perform UWB imaging that could be affected by the different design and construction of the antenna and not just its bandwidth, the same imaging setup for SWB imaging is employed for UWB imaging, and the same subtraction technique is utilized where the recorded signals obtained using the healthy phantom are subtracted from those using the unhealthy phantom. However, the range of frequency sweep is changed to reflect an ultra-wide bandwidth. Specifically, we utilize the following frequency ranges: (i) 3.1–40 GHz with 171.23% fractional bandwidth (FBW) for SWB imaging as in our earlier sections; and (ii) 3.1–10 GHz with 105.3% FBW for UWB imaging in this work. This choice of frequency range for UWB imaging is based on recommendations from previous studies on lung and other deep tumor detection [33], [51]. The designed SWB antenna has an impedance bandwidth of 36.9 GHz ($|S_{11}| < -10$ dB), peak realized gain of 3.5 – 6.2 dBi, stable omnidirectional radiation pattern, 97% radiation efficiency, and low cross-polarization level (< –40 dB) within the selected ultra-wide bandwidth.

For a proper comparison between images reconstructed using different imaging bandwidths (SWB and UWB), we employ the SCR metric, which is defined as the ratio of tumor intensity to the clutter intensity in the reconstructed image. Fig. 12 and Fig. 13 show the reconstructed images of both cases by DAS, and DMAS algorithm, respectively. The images by SWB imaging have clearer tumor indication and less clutter (light blue and green shades) than those by UWB imaging, affirming that the super-wide bandwidth has enhanced the spatial resolution of the images.

The results in Table IV quantify this enhancement. It shows that SWB imaging can outperform UWB imaging in terms of SCR by up to 84.4%.

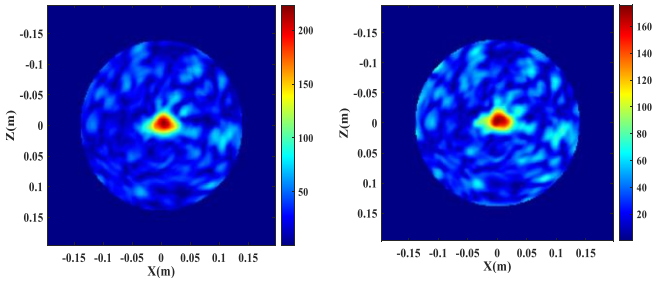

(a) (b)

Fig. 12. Reconstructed images of lung tumor using DAS by: (a) SWB imaging; and (b) UWB imaging

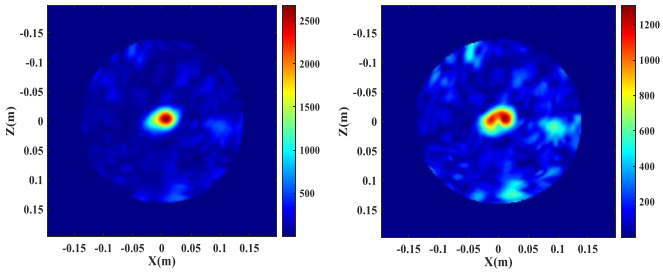

(a) (b)

Fig. 13. Reconstructed images of lung tumor using DMAS by: (a) SWB imaging; and (b) UWB imaging

TABLE IV
SCR OF SWB AND UWB IMAGING OF LUNG TUMOR

Beamforming algorithm	SCR of SWB (dB)	SCR of UWB (dB)	Percentage Improvement
DAS	13.97	9.5	47.1%
DMAS	26	14.1	84.4%

V. CONCLUSION

This paper investigates the capabilities of the SWB imaging approach for tumor detection at different depths, including deep-seated lung and in-situ skin tumors. Additionally, it investigates the dielectric properties of tissue-mimicking materials across the SWB frequency range of 3.1 to 40 GHz. Experimental measurements conducted using a life-size torso phantom with five tissue layers demonstrated the successful detection of lung and skin tumors. Furthermore, the imaging results show 47.1% and 84.4% enhancement in SCR over the UWB imaging approach when reconstructed using the DAS, and DMAS algorithms, respectively.

While our approach has shown promise, we acknowledge that there are limitations to this work. Firstly, the constructed phantoms do not entirely replicate the heterogeneous nature of the human torso. For instance, other anatomical structures such as the pleura and blood vessels are not mimicked in our torso model. Furthermore, we have not evaluated the detection of multiple tumors at different locations. Hence, as future work, we plan to address these limitations. We also plan to conduct animal testing and clinical trials to further prove the efficacy and safety of our SWB imaging approach.

REFERENCES

[1] R. C. Conceição, J. J. Mohr, and M. O'Halloran, *An introduction to microwave imaging for breast cancer detection* Basel, Switzerland: Springer International Publishing, 2016, pp. 41.

[2] R. Chandra, I. Balasingham, H. Zhou, and R. M. Narayanan, "Medical microwave imaging and analysis," In *Medical Image Analysis and Informatics*, CRC Press, pp. 451-466, 2017.

[3] W. Alamro, and B.-C. Seet, "Review of practical antennas for microwave and millimetre-wave medical imaging," In Electromagnetic Waves and Antennas for Biomedical Applications, 1st ed., Wang, L. Eds., IET The Institution of Engineering and Technology: UK, 2021, pp. 185-207.

[4] L. Wang, "Multi-frequency holographic microwave imaging for breast lesion detection," *IEEE Access*, vol. **7**, pp. 83984-83993, 2019.

[5] E. Porter, H. Bahrami, A. Santorelli, B. Gosselin, L. A. Rusch, et al., "A wearable microwave antenna array for time-domain breast tumor screening," *IEEE transactions on medical imaging*, vol. 35, no. 6, pp. 1501-1509, 2016.

[6] L. Wang, "Terahertz imaging for breast cancer detection," *Sensors*, vol. 21, no. 19, pp. 6465, 2021.

[7] W. -C. Lai, L. Guo, K. Bialkowski and A. Bialkowski, "An Explainable Deep Learning Method for Microwave Head Stroke Localization," *IEEE Journal of Electromagnetics, RF and Microwaves in Medicine and Biology*, vol. 7, no. 4, pp. 336-343, Dec. 2023.

[8] J. A. Tobon Vasquez, R. Scapaticci, G. Turvani, G. Bellizzi, D. O. Rodriguez-Duarte, et al., "A Prototype Microwave System for 3D Brain Stroke Imaging," *Sensors*, vol. 20, pp. 2607, 2020.

[9] B. Sohani, B. Khalesi, N. Ghavami, M. Ghavami, S. Dudley, et al., "Detection of haemorrhagic stroke in simulation and realistic 3-D human head phantom using microwave imaging," *Biomedical Signal Processing and Control*, vol. 61, pp. 102001, 2020.

[10] R. Inum, M. Rana, K. N. Shushama, and A. Quader, "EBG Based Microstrip Patch Antenna for Brain Tumor Detection via Scattering Parameters in Microwave Imaging System," *International Journal of Biomedical Imaging*, vol. 12. 2018.

[11] A. Darvazehban, S. A. Rezaeieh, A. Zamani, and A. M. Abbosh, "Pattern Reconfigurable Metasurface Antenna for Electromagnetic Torso Imaging," *IEEE Transactions on Antennas and Propagation*, vol. 67, no. 8, pp. 5453-5462, 2019.

[12] A. Darvazehban, S. A. Rezaeieh, and A. Abbosh, "Pattern-Reconfigurable Loop–Dipole Antenna for Electromagnetic Pleural Effusion Detection," *IEEE Transactions on Antennas and Propagation*, vol. 68, no. 8, pp. 5955-5964, 2020.

[13] S. A. Rezaeieh, A. Zamani, K. S. Bialkowski, A. Mahmoud, and A. M. Abbosh, "Feasibility of Using Wideband Microwave System for Non-Invasive Detection and Monitoring of Pulmonary Oedema," *Sci Rep*, vol. 5, pp. 14047, 2015.

[14] J. Z. Lim, S. L. Misra, A. Gokul, P. W. Hadden, A. Cavadino, et al., "Conjunctival Melanoma in Aotearoa—New Zealand: A 21-Year Analysis of Incidence and Survival," *The Asia-Pacific Journal of Ophthalmology*, vol. 12, no. 3, pp. 273-278, 2023.

[15] N. Pandeya, C. M. Olsen, M. M. Shalit, J. C. Dusingize, R. E. Neale, et al., "The diagnosis and initial management of melanoma in Australia: findings from the prospective, population-based QSkin study," *Medical Journal of Australia*, 2023.

[16] L. Beckert, and G. Laking, "All the cancer you cannot see," *The New Zealand Medical Journal, Te ara tika o te hauora hapori*, vol. 135, 14556, 2022.

[17] M. B. Amin, F. L. Greene, S. B. Edge, C. C. Compton, J. E. Gershenwald, et al., "The Eighth Edition AJCC Cancer Staging Manual: Continuing to build a bridge from a population-based to a more "personalized" approach to cancer staging," CA: *A Cancer Journal for Clinicians*, vol. 67, no. 2, pp. 93–99, 2017.

[18] N. Bao, Y. Chen, Y. Liu, and C. Chakraborty, "Multi-objective path planning for lung biopsy surgery," *Multimedia Tools and Applications*, pp.1-18, 2022.

[19] L. Wang, and A. M. Al-Jumaily, "Imaging of Lung Structure Using Holographic Electromagnetic Induction,'' *IEEE Access*, vol. 5, pp. 20313-20318, 2017.

[20] A. Zamani, S. Rezaeieh, and A. Abbosh, "Lung cancer detection using frequency-domain microwave imaging," *Electronics Letters*, vol. 51, no. 10, pp. 740-741, 2015.

[21] A. Ahmed, V. Kumari, and G. Sheoran, "Experimental investigation of microwave holographic reflectometry for lung tumor detection," *Measurement*, vol. 197, pp. 111336, 2022.

[22] B. Khalesi, B. Khalid, N. Ghavami, G. Raspa, M. Ghavami, et al., "A Microwave Imaging Procedure for Lung Lesion Detection: Preliminary Results on Multilayer Phantoms," *Electronics*, vol. 11, no. 13, pp. 2105, 2022.

[23] A. Alhawari, "Lung tumour detection using ultra-wideband microwave imaging approach," *Journal of Fundamental and Applied Sciences*, vol. 10, no. 2, 2018.

[24] W. Ameer, D. Awan, S. Bashir, and A. Waheed, "Use of Directional UWB Antenna for Lung Tumor Detection," In *Proc. 2nd International Conference on Advancements in Computational Sciences (ICACS)*. Lahore, Pakistan, 18–20 February 2019.

[25] M. M. Abdelhamid, and A. M. Allam, "Detection of Lung Cancer Using Ultra Wide Band Antenna," In *Proc. Loughborough Antennas & Propagation Conference (LAPC)*. Loughborough, UK, 14–15 November 2016.

[26] A. Mirbeik-Sabzevari, S. Li, E. Garay, H.-T. Nguyen, H. Wang, et al., "Synthetic ultra-high-resolution millimeter-wave imaging for skin cancer detection," *IEEE Transactions on Biomedical Engineering*, vol. 66, no. 1, pp. 61-71, 2018.

[27] K. Kaur, and A. Kaur, "In vitro detection of skin cancer using an UWB stacked micro strip patch antenna with microwave imaging," *International Journal of RF and Microwave Computer-Aided Engineering*, vol. 32, no. 12, e23407, 2022.

[28] A. M. Tripathi, P. K. Rao, and R. Mishra, "An AMC inspired wearable UWB antenna for skin cancer detection," In *Proc. International Conference on Electrical and Electronics Engineering (ICE3)*, Gorakhpur, India, 14–15 February 2020.

[29] B. Khalesi, G. Tiberi, N. Ghavami, M. Ghavami, and S. Dudley, "Skin cancer detection through microwaves: validation on phantom measurements," In *Proc. IEEE International Conference on Imaging Systems and Techniques*, Krakow, Poland, 16–18 October 2018.

[30] S. Alani, Z. Zakaria, T. Saeidi, A. Ahmad, M. A. Imran, et al., "Microwave imaging of breast skin utilizing elliptical UWB antenna and reverse problems algorithm," *Micromachines*, vol. 12, no. 6, pp. 647, 2021.

[31] S. Bing, K. Chawangand, and J. C. Chiao, "A Tuned Microwave Resonant Sensor for Skin Cancerous Tumor Diagnosis," *IEEE Journal of Electromagnetics, RF and Microwaves in Medicine and Biology*, vol. 6, no. 4, pp. 320–327, 2023.

[32] W. Alamro, B.-C. Seet, L. Wang and P. Parthiban, "Compact super-wideband antenna for medical imaging applications," In *Proc. IEEE Conference on Antenna Measurements & Applications (CAMA)*, Antibes Juan-les-Pins, France, 15–17 November 2021.

[33] W. Alamro, B.-C. Seet, L. Wang and P. Parthiban, "Early-Stage Lung Tumor Detection Based on Super-Wideband Microwave Reflectometry," *Electronics*, vol. 12, no. 1, article 36, 2023.

[34] B. Sohani, A. D. Abdallah, G. Tiberi, N. Ghavami, M. Ghavami, et al., "An analytically based approach for evaluating the impact of the noise on the microwave imaging detection," In *Proc. Photonics & Electromagnetics Research Symposium (PIERS)*, Hangzhou, China, 21-25 November 2021.

[35] M. A. Elahi, B. R. Lavoie, E. Porter, M. Olavini, E. Jones, et al., "Comparison of radar-based microwave imaging algorithms applied to experimental breast phantoms," In *Proc. XXXIInd General Assembly and Scientific Symposium of the International Union of Radio Science (URSI GASS)*, Montreal, QC, Canada, 19–26 August 2017.

[36] S. Jacobsen, and Y. Birkelund, "Improved resolution and reduced clutter in ultra-wideband microwave imaging using cross-correlated back projection: Experimental and numerical results," *Journal of Biomedical Imaging*, vol. 2010, article 781095, 2011.

[37] A. L. de Paula, M. C. Rezende, and J. J. Barroso, "Modified Nicolson-Ross-Weir (NRW) method to retrieve the constitutive parameters of low-loss materials," In *Proc. SBMO/IEEE MTT-S International Microwave and Optoelectronics Conference (IMOC)*, Natal, Brazil, 29 October – 01 November 2011.

[38] E. J. Rothwell, J. L. Frasch, S. M. Ellison, P. Chahal, and R. O. Ouedraogo, "Analysis of the Nicolson-Ross-Weir method for characterizing the electromagnetic properties of engineered materials," *Progress in Electromagnetics Research*, vol. 157, pp. 31–47, 2016.

[39] C. Gabriel, S. Gabriel, and Y. Corthout, "The dielectric properties of biological tissues: I. Literature survey," *Physics in medicine & biology*, vol. 41, no. 11, pp. 2231, 1996.

[40] K. Sasaki, K. Wake, and S. Watanabe, "Development of best fit Cole-Cole parameters for measurement data from biological tissues and organs between 1 MHz and 20 GHz," *Radio Science*, vol. 49, no. 7, pp. 459–472, 2014.

[41] S. L. Vieira, T. Z. Pavan, J. E. Junior, and A. A. O. Carneiro, "Paraffin-gel tissue-mimicking material for ultrasound-guided needle biopsy phantom," *Ultrasound in medicine & biology*, vol. 39, no. 12, pp. 2477–2484, 2013.

[42] D. Shrotriya, R. S. Yadav, R. N. L. Srivastava, and T. R. Verma, "Design and development of an indigenous in-house tissue-equivalent female pelvic phantom for radiological dosimetric applications," *Iranian Journal of Medical Physics*, vol. 15, no. 3, pp. 200–205, 2018.

[43] R. B. Holmes, I. S. Negus, S. J. Wiltshire, G. C. Thorne, and P. Young, "Creation of an anthropomorphic CT head phantom for verification of image segmentation," *Medical Physics*, vol. 47, no. 6, pp. 2380–2391, 2020.

[44] A. M. Ali, P. Hogg, S. Johansen, and A. England, "Construction and validation of a low cost paediatric pelvis phantom," *European Journal of Radiology*, vol. 108, pp. 84–91, 2018.

[45] T. N. Tulasidas, G. S. V. Raghavan, F. van de Voort and R. Girard, "Dielectric Properties of Grapes and Sugar Solutions at 2.45 GHz," *Journal of Microwave Power and Electromagnetic Energy*, vol. 30, no. 2, pp. 117-123, 1995.

[46] L. Wang, R. Simpkin, and A. Al-Jumaily, "Three-dimensional holographic microwave imaging array: experimental investigation of tumour detection in breast phantom," In *Proc. ASME International Mechanical Engineering Congress and Exposition*, San Diego, CA, USA, 15–21 November 2013.

[47] M. Ahadi, J. Nourinia, and C. Ghobadi, "Square Monopole Antenna Application in Localization of Tumors in Three Dimensions by Confocal Microwave Imaging for Breast Cancer Detection: Experimental Measurement," *Wireless Pers Commun*, vol. 116, pp. 2391–2409, 2021.

[48] J. R. Wang, B. Y. Sun, H. X. Wang, S. Pang, X. Xu, and Q. Sun, "Experimental study of dielectric properties of human lung tissue in vitro," *Journal of Medical and Biological Engineering*, vol. 34, no. 6, pp.598-604, 2014.

[49] L. Farina, G. Ruvio, R. Shatwan, A. Shalaby, M. O'Halloran, A. White, A. Soo, D. Breen, A. Lowery, and A. M. Quinn, "Histology-Validated Dielectric Characterisation of Lung Carcinoma Tissue for Microwave Thermal Ablation Applications," *Cancers (Basel)*, 2023 vol. 15, no. 14, pp. 3738, 2023.

[50] M. A. Elahi, D. O'Loughlin, B. R. Lavoie, M. Glavin, E. Jones, E. C. Fear, M. O'Halloran, "Evaluation of Image Reconstruction Algorithms for Confocal Microwave Imaging: Application to Patient Data," *Sensors*, vol. 18, pp. 1678, 2018.

[51] A. Hossain, M. T. Islam, M. E. H. Chowdhury, H. Rmili, and M. Samsuzzaman, "A planar ultrawideband patch antenna array for microwave breast tumor detection," *Materials*, vol. 13, article 4918, 2020.

[52] K. C. Yaw, "Measurement of dielectric material properties," Rohde & Schwarz, Munich, Germany, Appl. Note 04.2012-RAC0607-0019-1-4E, 2012.

Wasan Alamro (Member, IEEE) received her B.E. (First Class Honors) degree in electrical engineering - telecommunication from Mu'tah University, Jordan, and M.S. degree in electrical engineering - wireless communication from University of Jordan, Amman, Jordan, in 2014, and 2018, respectively. From 2018 to 2022, she worked as a spectrum assignment and licensing engineer with telecommunication regulatory commission, Jordan. She is currently pursuing her Ph.D. degree in electrical engineering at Auckland University of Technology, New Zealand. Her research interests include antenna design and microwave imaging systems.

Boon-Chong Seet (Senior Member) received his Ph.D. degree from Nanyang Technological University, Singapore, in 2005. After graduation, he was a Research Fellow under the Singapore Massachusetts Institute of Technology Alliance (SMA) Program with the National University of Singapore. Since December 2007, he has been with the Department of Electrical and Electronic Engineering, Auckland University of Technology, New Zealand, where he is currently a Professor and Head of the Department. His research activities span the fields of information and communication technologies (ICT), including antennas and radio frequency based sensors for biomedical applications.

Lulu Wang (Member, IEEE) received her Ph.D. degree from Auckland University of Technology, New Zealand in 2013. She is currently a Distinguished Professor of biomedical engineering at Shenzhen Technology University, China, and was named one of the world's top 2% scientists by Stanford University in 2021. Dr. Wang is an active editor and reviewer of numerous journals, books, and conferences. She has given numerous invited talks at national and international conferences. She has also received multiple national and international awards from various professional societies and organizations.

Prabakar Parthiban (Member, IEEE) received his Ph.D. degree from Auckland University of Technology, New Zealand, in 2020. He is currently employed as an Advanced Wireless/RF Engineer with Honeywell Aerospace, United Kingdom. He has more than 13 years of industrial work experience in full-duplex transceiver front-ends and passive & active antenna design, testing and commercialization along with compliance and regulatory know-how. His current research interests are in mm-Wave Space and Satellite Communications, IoT, RAIN RFID, and other Auto-ID technologies.